

Crystallization behaviors and microstructures of poly(butylene succinate-co-adipate)/modified layered double hydroxide nanocomposites

Yi-An Chen¹ · Gang-Shian Tsai¹ · Erh-Chiang Chen¹ · Tzong-Ming Wu¹

Received: 8 November 2015 / Accepted: 2 January 2016 / Published online: 11 January 2016
© Springer Science+Business Media New York 2016

Abstract A green biodegradable poly[(butylene succinate)-co-adipate] (PBSA) synthesized by polycondensation reaction is solution-mixed with organically modified layered double hydroxide (m-LDH) to fabricate the PBSA/m-LDH nanocomposite. The crystallization behaviors, morphologies, and microstructures of PBSA and PBSA/m-LDH nanocomposite are studied by differential scanning calorimetry, wide-angle X-ray diffraction (WAXD), transmission electron microscopy (TEM), and small-angle X-ray scattering (SAXS). Both WAXD and TEM results demonstrate that most of the layered materials are exfoliated and randomly distributed in the PBSA matrix. The isothermal crystallization kinetics of neat PBA and PBSA/m-LDH nanocomposite are analyzed using the Avrami equation. With the addition of 3 wt% m-LDH into PBSA, the half-time for crystallization of PBSA/m-LDH nanocomposite decreased by 47–76 % for isothermal crystallization at 48–56 °C compared to that of neat PBSA. The value of $\sigma\sigma_e$ for 3 wt% PBSA/m-LDH nanocomposites is the lowest. The microstructure of PBSA/m-LDH nanocomposites identified by SAXS shows that higher crystal layer thickness is achieved with the introduction of 3 wt% m-LDH. These results indicate that the introduction of 3 wt% m-LDH content into PBSA causes a decrease in surface free energy and thus an increase in the polymer chain mobility.

Introduction

Biodegradable polymers, such as poly(butylene succinate) (PBS), poly[(butylene succinate)-co-adipate] (PBSA), and poly(L-lactic acid) (PLLA), have been attracting much research interest from academic and industrial perspectives [1–12]. PBSA, a semi-crystalline aliphatic copolyester with random comonomer sequence, is synthesized by polycondensation of 1,4-butanediol in the presence of succinic acids (SA) and adipic acids (AA) [2–4]. PBSA has been widely used in life and biomedical applications, including the manure and waste compost, agricultural packing, and food industry [13–15]. However, due to the more flexible macromolecular chains, slower crystallization rate, and lower crystallinity of PBSA, practical application has been limited [7]. In order to overcome these drawbacks, the addition of inorganic layered material into the biodegradable polymers as reinforcement materials could help in enhancing its physical properties, crystallization rate, and crystallinity [6, 16–22].

Layered double hydroxides (LDHs) belonging to a class of two-dimensional layered material have been widely investigated [6, 17–22]. In recent times, the polymer/LDH nanocomposites have been recognized as one of the most promising research field due to the incorporation of nanofillers with numerous sizes and shapes [6, 17–22]. Most studies lay emphasis on polymer/LDHs nanocomposites, which after exfoliation and intercalation within the polymer structure, derive great enhancement in their physical properties [6, 17–22]. The interlayer spacing of original LDHs is too small to allow for the intercalation of polymer chains into their interlayer gallery unless the gallery is greatly increased [6, 17–22]. In order to overcome this difficulty, several studies have utilized organo-modifiers to function as delamination compounds of LDHs [6, 17–22].

✉ Tzong-Ming Wu
tmwu@dragon.nchu.edu.tw

¹ Department of Materials Science and Engineering, National Chung Hsing University, 250 Kuo Kuang Road, Taichung 4021, Taiwan

Because of the application of green nanocomposites, the organo-modifiers should possess biocompatible and non-toxic properties. In this work, we utilize the biocompatible oleic acid and sorbitol as organo-modifiers to fabricate the organically modified LDHs (hereafter designated as m-LDH) by one-step co-precipitation method.

The rheological behavior, nonisothermal crystallization, and microstructure of PBSA with inorganic layered materials, such as Montmorillonite (MMT), Cloisite 30B (C30B), and Cloisite 25A (C25A), have been investigated extensively [1, 7–11]. However, the effects of the LDHs on the isothermal crystallization behavior and microstructure of PBSA have not yet been discussed. In this study, the PBSA/m-LDH nanocomposites have been fabricated, and the morphology, microstructure, and crystallization behavior of isothermally crystallized PBSA/m-LDH nanocomposites are investigated.

Experimental

Materials

Titanium (IV) isopropoxide, AA, and sorbitol were purchased from Sigma-Aldrich Chemical Company. SA and chloroform were obtained from J. T. Baker Chemical Company. Oleic acid, $\text{Mg}(\text{NO}_3)_2 \cdot 6\text{H}_2\text{O}$ (97 %), and $\text{Al}(\text{NO}_3)_3 \cdot 9\text{H}_2\text{O}$ (98 %) were acquired from Showa Chemicals Corp. All agents were used as received without further purification.

Sample preparation

Preparation of LDH and m-LDH

According to the previously published method, the LDH and m-LDH powders were prepared [17]. The interlayer distances of LDH and m-LDH were 8.3 and 58.8 Å, respectively.

Synthesis of PBSA

The synthesis of PBSA copolymer has been used by previous investigations [2–4]. The feed molar ratio of SA to AA was 75:25. 1,4-Butanediol and dicarboxylic acid were added with a mol ratio of 1:1.10. Titanium (IV) isopropoxide as catalyst was used. To avoid oxidation and remove the air during the transesterification, the reactor with the monomers was emptied and filled with N_2 gas. The reaction under constant N_2 gas flow was heated at 190 °C for 2 h and mechanically stirred at 400 rpm. For the deglycolization, the pressure was depressed steadily to below 67 Pa over 8 h at the reaction temperature of 220 °C. The PBSA copolymer was dissolved in chloroform and precipitated in excess methyl alcohol (anhydrous) to

retain oligomers and remove unreacted monomers. The purified PBSA copolymer was filtrated and then vacuum dried at 40 °C for 3 days. The weight-averaged molecular weight of PBSA determined using gel permeation chromatography was estimated to be 3.4×10^{-4} g/mol.

Fabrication of the PBSA/m-LDH nanocomposites

The PBSA/m-LDH nanocomposites were prepared by the solution intercalation method. PBSA and m-LDH were separately dissolved in 20 ml chloroform for 3 h. The various concentrations (1, 3, and 5 wt%) of m-LDH solution were added into the PBSA solution and kept mechanically stirred at 250 rpm for 8 h. The various concentrations of PBSA/m-LDH solution were cast on an aluminum plate at 25 °C for 24 h. The residual solvent was removed by drying under vacuum at 40 °C for 24 h.

Wide-angle X-ray diffraction (WAXD)

Wide-angle X-ray diffraction (WAXD) was performed on a Bruker D8 diffractometer equipped with Ni-filtered Cu K_α radiation in the reflection mode. X-ray diffraction patterns were recorded from $2\theta = 1.5^\circ\text{--}40^\circ$ at a scan rate of $1^\circ/\text{min}$.

Small-angle X-ray scattering (SAXS)

The small-angle X-ray scattering (SAXS) experiments were performed using the Bruker D8 Discover equipped with Ni-filtered Cu K_α radiation in the transmission mode. The distance from sample to detector was ~ 30 cm. The scattering vector (q , nm^{-1}) is defined as $q = (4\pi\sin\theta)/\lambda$, where λ and 2θ are the wavelength and the scattering angle, respectively.

Transmission electron microscopy (TEM)

The ultrathin sections were prepared by sectioning the sample at room temperature. Transmission electron microscopy (TEM) performed on a Hitachi HF-2000 at 200 kV was used to characterize the distribution of m-LDH within the PBSA/m-LDH nanocomposites. In order to observe the stacked m-LDH within the polymer matrix, the sample was immobilized in epoxy resin. Then, the resin-embedded samples were microtomed at room temperature using a Reichert Ultracut ultramicrotome equipped with a diamond knife. The slices were collected on carbon-coated copper grid.

Differential scanning calorimeter (DSC)

The isothermal crystallization behavior was characterized by means of a PerkinElmer Pyris Diamond DSC calibrated

using indium. All samples were heated to 150 °C at a rate of 10 °C/min under a nitrogen atmosphere and held there for 5 min to erase the thermal history. Subsequently, the samples were rapidly cooled to the specified isothermal crystallization temperatures (T_{cs}), and held at this temperature to allow complete crystallization. The proposed T_{cs} values are selected in the range between 48 and 56 °C.

Polarizing optical microscopy (POM)

Ultrathin sections of samples were observed under a Zeiss optical microscope equipped with crossed polarizer to support the isothermal crystallization results analyzed by DSC. All samples were placed inside the Mettler FP-82 hot stage, and the temperature was raised to 150 °C at the rate of 10 °C/min to eliminate the previous thermal history, and held at that temperature for 5 min. Subsequently, the samples were then cooled quickly to the proposed T_{cs} . The crystallization evolutions of PBSA/m-LDH nanocomposites were recorded at the specified T_{cs} for various durations.

Nuclear magnetic resonance (NMR)

$^1\text{H-NMR}$ spectra were recorded on VARIAN INOVA 600 MHz NMR spectrometer using CDCl_3 as solvent and internal standard.

Results and discussion

Synthesis and characterization of PBSA copolymer

PBSA copolymer was synthesized by a two-stage polycondensation reaction. The first step consists of transesterification reaction. The reaction was carried out at a temperature of 190 °C at normal pressure with stoichiometric excess of 1,4-butanediol in the presence of a transition metal complex. Then, the reaction was performed by heating the mixture at 220 °C for 8 h under vacuum to remove the excess 1,4-butanediol and hence produce chain extension. Figure 1 presents the $^1\text{H-NMR}$ spectrum of PBSA copolymer. The $^1\text{H-NMR}$ spectrum of the PBSA copolymer is shown: $-\text{CH}_2-$, from the 1,4-butanediol unit and the adipoyl unit at $\delta = 1.72$; COCH_2- , from the adipoyl unit at $\delta = 2.33$; COCH_2- , from the succinyl unit at $\delta = 2.63$; OOCH_2- , from the 1,4-butanediol unit at $\delta = 4.13$. The observed $^1\text{H-NMR}$ spectrum is consistent with the chemical structure of PBSA [2–4]. The molar composition of PBSA copolymer was measured as the area ratio of $\delta = 2.63$ and $\delta = 2.33$ peaks [2–4]. The theoretical values of SA and AA are 75 and 25 mol%, respectively. In fact, the SA residues incorporated into the PBSA copolymer are about 2 mol% less than the actual amount

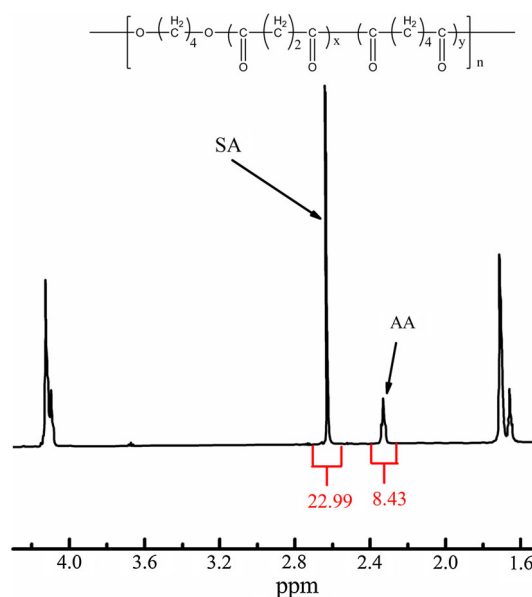


Fig. 1 $^1\text{H-NMR}$ spectrum of the PBSA copolymer ([SA]/[AA] = 75/25)

expected from the reaction mixture compositions, which falls within the limits of experimental error. This result indicates that the concentration of the PBSA copolymer is in agreement with those expected from the feed.

Structure and morphology of PBSA and PBSA/m-LDH nanocomposites

Figure 2a and f show the WAXD patterns of LDH and m-LDH. The interlayer spacing d_{003} values of LDH and m-LDH determined using the strong diffraction peaks at

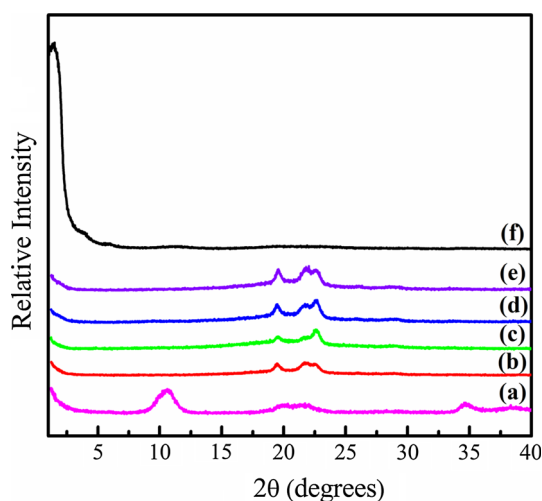


Fig. 2 WAXD patterns of (a) LDH, (b) PBSA, (c) 1 wt% PBSA/m-LDH, (d) 3 wt% PBSA/m-LDH, (e) 5 wt% PBSA/m-LDH nanocomposites, and (f) m-LDH

$2\theta = 10.6^\circ$ and 1.4° are 8.3 and 58.8 Å, respectively. It is clear that the interlayer spacing of LDH is significantly increased with oleic acid and sorbitol through the ionic exchange [17]. As shown in Fig. 2b, the diffraction peaks of PBSA at $2\theta = 19.4^\circ$, 21.5° , and 22.5° are corresponding to (020), (021), and (110) crystallographic planes of PBSA, respectively. These data indicate that the crystal structure of PBSA is the same as that of PBS [2–4]. For the samples of nanocomposites, the diffraction peaks at $2\theta = 19.4^\circ$, 21.5° , and 22.5° are also observed, which are attributed to the crystalline structure of PBSA. No diffraction peak of m-LDH appears in the nanocomposite samples. Therefore, the complete disappearance of the basal plane of LDH may be due to the absence of regular periodicity of the stacked lamellar m-LDH structure, leading to the formation of exfoliated and disordered nanostructure within the PBSA matrix. Consequently, the m-LDH platelets are randomly dispersed throughout the PBSA matrix.

Although WAXD provides a theoretical implication on the distribution of the nanofiller and the disappearance of the diffraction peak corresponds to larger d-spacing or collapse of the stacked lamellar structure of m-LDH, a complete characterization of nanocomposite morphology requires microscopic investigation. Therefore, the morphology of m-LDH in the PBSA matrix was observed by TEM. Figure 3 presents TEM micrographs of 5 wt% PBSA/m-LDH nanocomposites. The gray areas represent the polymer matrix, whereas dark lines correspond to the LDH layers. The high magnification of TEM image is shown in Fig. 3b. The observation clearly reveals that m-LDH layers are inhomogeneously distributed in the continuous PBSA matrix and have completely lost their stacking orders. These results indicate that the original stacked lamellar structure of m-LDH can be modified to form the disorderly dispersed morphology in the PBSA

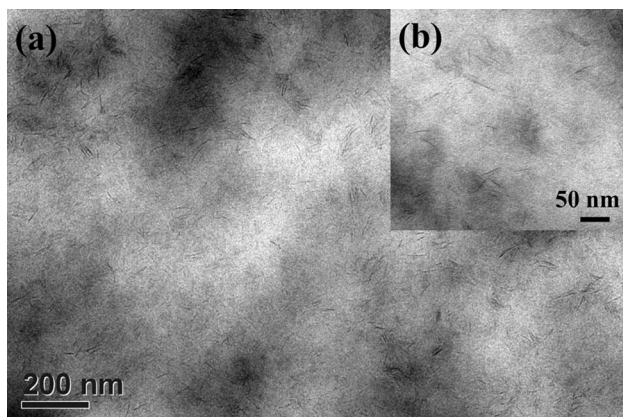


Fig. 3 TEM micrographs obtained from the embedded and cutted 5 wt% PBSA/m-LDH nanocomposite (a) low magnification, (b) high magnification

matrix. Accordingly, the exfoliated morphology observed by TEM is in good agreement with the WAXD results.

Isothermal crystallization behaviors of PBSA and PBSA/m-LDH nanocomposites

In order to elucidate the effects of crystallization temperature (T_c) on crystallization behaviors of PBSA and PBSA/m-LDH nanocomposites, isothermal crystallization of PBSA matrix with different m-LDH contents were investigated. Isothermal crystallization kinetics was analyzed by means of Avrami equation. The equation can be described as follows [23, 24]:

$$1 - X_t = \exp(-kt^n), \quad (1)$$

where X_t is relative degree of crystallinity at crystallization time t , k is the crystallization rate constant, and n is the Avrami exponent. To convert conveniently with the operation, Eq. (1) can be transformed into its natural logarithm form as given in Eq. (2).

$$\ln[-\ln(1 - X_t)] = n \ln t + \ln k. \quad (2)$$

The crystallization half-time ($t_{1/2}$) is the time at which the extent of crystallization is 50 %, which is defined in Eq. (3).

$$t_{1/2} = \left(\frac{\ln 2}{k}\right)^{1/n}. \quad (3)$$

The Avrami plots of PBSA and PBSA/m-LDH nanocomposites are presented in Fig. 4. All curves are almost parallel to each other, indicating that the crystallization mechanisms of the PBSA and PBSA/m-LDH nanocomposites at different T_{cs} remain the same. For comparison, the n -values, k -values, and $t_{1/2}$ at different T_{cs} are listed in Table 1. In the Avrami expression, the n -value presents qualitative information on the mechanism of nucleation and the formation of crystal growth. From Table 1, it can be observed that the n -values of PBSA are found to be ranging from 2.84 to 3.08. The nonintegral n -values suggest the presence of crystalline branching during crystallization, a mixed nucleation and growth mechanism, and two-stage crystal growth [25, 26]. In general, the n -values close to 3 are attributed to an athermal nucleation process followed by a three-dimensional crystal growth and homogeneous nucleation mechanism. The n -values of PBSA/m-LDH nanocomposites are in the range of 2.51–3.28, which are close to those of PBSA. Therefore, these results suggest that the introduction of m-LDH into the PBSA matrix does not change the crystallization mechanism of PBSA. In addition, it is not appropriate to compare the overall crystallization rate from the k -values directly because the unit of k is min^{-n} and n is not constant in this study for all the samples at different T_{cs} values.

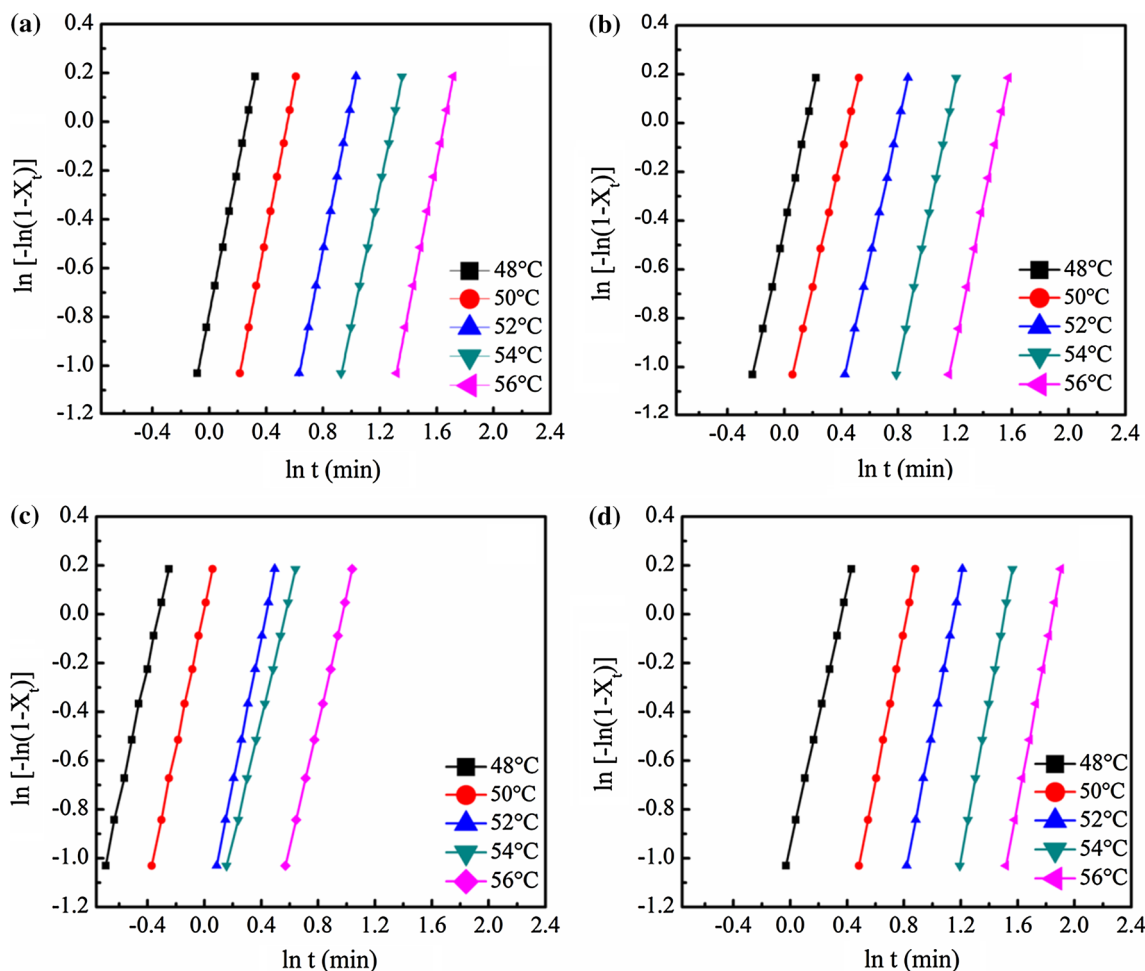


Fig. 4 Avrami plots of **a** PBSA, **b** 1 wt% PBSA/m-LDH, **c** 3 wt% PBSA/m-LDH, **d** 5 wt% PBSA/m-LDH nanocomposites

Thus, the $t_{1/2}$ is employed to discuss the crystallization kinetics of neat PBSA and PBSA/m-LDH nanocomposites. As shown in Table 1, $t_{1/2}$ increases with the increasing T_c for the all samples, suggesting that the isothermal crystallization rate decreases with the increasing T_c , due to the low supercooling at higher T_c . By adding more m-LDH into PBSA up to 3 wt%, the $t_{1/2}$ slightly decreases as the content of m-LDH increases. For example, the $t_{1/2}$ values of PBSA decrease remarkably from 4.64 to 1.48 min in nanocomposites with the addition 3 wt% m-LDH when crystallized at equal difference between T_m^0 and T_c . This implies that m-LDH accelerates the crystallization of PBSA in the nanocomposites. However, with the addition of 5 wt% m-LDH, the $t_{1/2}$ for crystallization of the PBSA/m-LDH nanocomposite increased more compared to that of 3 wt% PBSA/m-LDH nanocomposites. These results suggest that higher content of m-LDH would hinder the diffusion and migration of PBSA chains to the packing of crystals due to the restriction effects, resulting in the increase of $t_{1/2}$ values.

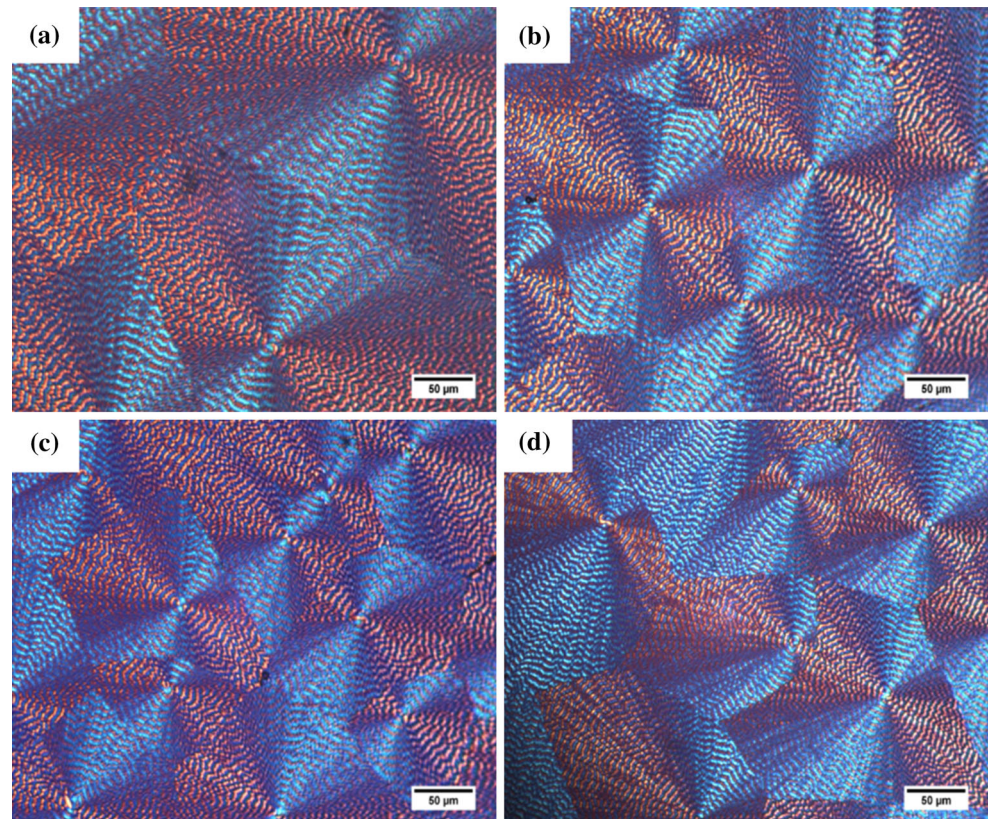
The crystalline morphologies and nucleation of the PBSA and PBSA/m-LDH nanocomposites were investigated by POM observation data to further reveal the crystallization behaviors of the PBSA and PBSA/m-LDH nanocomposites. Figure 5 shows the spherulite morphology of the samples isothermally crystallized at 52 °C. It is clear that the spherulite size of the PBSA/m-LDH nanocomposites decreases and the number of spherulites increases with the loading of 3 wt% m-LDH. The addition of 3 wt% m-LDH induces nucleation sites for PBSA crystallization and results in the restricted growth of PBSA spherulites. This implies that the incorporation of the m-LDH up to 3 wt% into PBSA could induce heterogeneous nucleation and change the crystallization behavior of PBSA. However, the spherulite size of 5 wt% PBSA/m-LDH nanocomposite becomes bigger, and the number of spherulites becomes less at the loading of 5 wt% m-LDH. This result indicates that high content of m-LDH can inhibit the molecular motion of PBSA chains due to the interaction of organic modifier and m-LDH, resulting in the decrease of nucleation.

Table 1 Kinetic parameters of neat PBSA and PBSA/m-LDH nanocomposites isothermally melt crystallized at $T_c = 48\text{--}56\text{ }^\circ\text{C}$

Sample	T_c ($^\circ\text{C}$)	ΔT ($^\circ\text{C}$)	n	k (min^{-n})	$t_{1/2}$ (min)	G ($\mu\text{m/s}$)
PBSA	48	53.5	3.00	0.455	1.15	0.333
	50	51.5	3.08	0.184	1.54	0.257
	52	49.5	3.04	0.052	2.35	0.246
	54	47.5	2.84	0.025	3.21	0.203
	56	45.5	3.05	0.006	4.64	0.173
1 wt% PBSA/m-LDH	48	51.1	2.74	0.652	1.02	0.291
	50	49.1	2.62	0.305	1.37	0.246
	52	47.1	2.74	0.111	1.95	0.209
	54	45.1	2.89	0.037	2.77	0.180
	56	43.1	2.93	0.012	4.01	0.146
3 wt% PBSA/m-LDH	48	50.5	2.72	2.394	0.63	0.282
	50	48.5	2.84	1.022	0.87	0.234
	52	46.5	2.96	0.277	1.36	0.198
	54	44.5	2.51	0.239	1.53	0.169
	56	42.5	2.59	0.081	2.29	0.137
5 wt% PBSA/m-LDH	48	49.9	2.62	0.387	1.25	0.343
	50	47.9	3.07	0.080	2.02	0.303
	52	45.9	3.11	0.028	2.82	0.232
	54	43.9	3.28	0.007	4.04	0.187
	56	41.9	3.16	0.003	5.64	0.140

ΔT the difference between T_m^0 and T_c

Fig. 5 Optical micrographs of the spherulitic morphology of **a** PBSA, **b** 1 wt% PBSA/m-LDH, **c** 3 wt% PBSA/m-LDH, **d** 5 wt% PBSA/m-LDH nanocomposites at $52\text{ }^\circ\text{C}$. (Scale $50\text{ }\mu\text{m}$)



The effects of the PBSA and PBSA/m-LDH nanocomposites on the spherulitic growth rate (G) were also investigated in the present study using POM data. Table 1 summarizes the G -values for PBSA and PBSA/m-LDH nanocomposites. It is found that the G -values of all the samples decreased with the increasing T_c , and the G -values decreased with the increasing weight fraction of m-LDH at a given T_c .

The linear Hoffman–Weeks equation was used to determine the equilibrium melting temperature (T_m^0) of PBSA and PBSA/m-LDH nanocomposites. The classical Hoffman–Weeks equation was employed [27, 28]:

$$T_m = T_m^0 \left(1 - \frac{1}{\gamma}\right) + \frac{T_c}{\gamma}, \tag{4}$$

where γ is the ratio of final to initial lamellar thickness. The T_m^0 values summarized in Table 2 can be obtained from the intersection of this line with the $T_m = T_c$ line. The T_m^0 values of neat PBSA and nanocomposites are calculated to be 101.47 °C for PBSA and 99.13, 98.48, and 97.87 °C for 1, 3, and 5 wt% loadings of m-LDH, respectively. The value of T_m^0 for PBSA/m-LDH nanocomposites is slightly lower than that of PBSA. These results suggest that the crystalline arrangement in PBSA/m-LDH nanocomposites is less perfect than that of PBSA. This phenomenon is probably due to the presence of more heterogeneous nucleation, which reduces the perfection in the formation of PBSA crystallites in PBSA/m-LDH nanocomposites, or greater restriction to the formation of PBSA crystals within the m-LDHs.

To obtain detailed information on the spherulitic growth rates of PBSA and PBSA/m-LDH nanocomposites, we further utilized Lauritzen–Hoffman theory [29].

$$G = G_0 \exp\left[\frac{-U^*}{R(T_c - T_\infty)}\right] \exp\left[\frac{-K_g}{fT_c \Delta T}\right], \tag{5}$$

where G_0 is a pre-exponential term, U^* is the activation energy for segment diffusion to the site of crystallization ($U^* = 6300 \text{ J mol}^{-1}$), T_∞ is the hypothetical temperature below which viscous flow ceases ($T_\infty = T_g - 30 \text{ K}$), $f = 2T_c/(T_m^0 + T_c)$ is a correction factor, and $\Delta T = T_m^0 - T_c$ is the degree of supercooling [27]. K_g is a nucleation constant, as depicted by

Table 2 Values of T_m^0 , K_g , and $\sigma\sigma_e$ at various T_c values for PBSA and PBSA/m-LDH nanocomposites

PBSA	T_m^0 (K)	K_g (K ²)	$\sigma\sigma_e$ (erg ² /cm ⁴)
PBSA	374.62	1.157×10^5	327.03
1 wt% PBSA/m-LDH	372.28	1.117×10^5	315.08
3 wt% PBSA/m-LDH	371.63	1.111×10^5	316.47
5 wt% PBSA/m-LDH	371.02	1.267×10^5	321.11

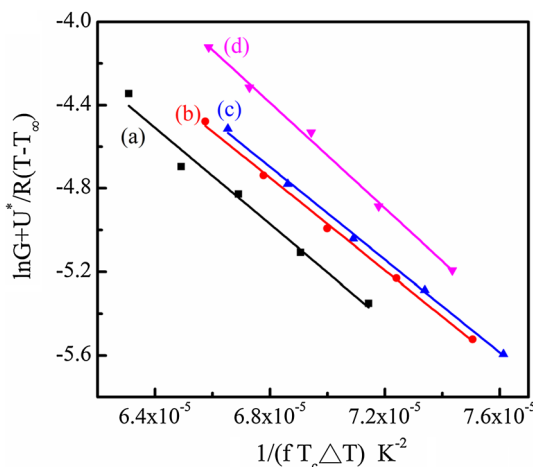


Fig. 6 The plot of $\ln G + U^*/R(T - T_\infty)$ versus $1/(fT_c \Delta T)$ for (a) PBSA, (b) 1 wt% PBSA/m-LDH, (c) 3 wt% PBSA/m-LDH, (d) 5 wt% PBSA/m-LDH nanocomposites

$$K_g = \frac{mb\sigma\sigma_e T_m^0}{k\Delta H_f^0}, \tag{6}$$

where b is the crystal layer thickness; σ and σ_e are the lateral and end-surface free energies, respectively; k is the Boltzmann constant, and ΔH_f^0 is the heat of fusion per unit volume. The parameter m applied in this equation is 4 in regimes I and III and 2 in regime II.

Figure 6 presents the relations between $[\ln(G) + U^*/R(T_c - T_\infty)]$ and $1/[fT_c \Delta T]$ for PBSA and PBSA/m-LDH nanocomposites. The values of crystal layer thickness (b) and heat of fusion per unit volume (ΔH_f^0) are 9.08 Å [4] and 113.4 J/g, respectively [4]. To determine whether the crystal growth occurs in regime I or II, the Z-test of Lauritzen is available. The Lauritzen Z-test equation is defined as [30]

$$Z \approx 10^3 \left(\frac{L}{2a_0}\right)^2 \exp\left(\frac{-X}{T_c \Delta T}\right), \tag{7}$$

where L is the effective lamellar width, and a_0 is the lattice constant. The regime I kinetics is followed, if substitution of $X = Kg$ leads to $Z \leq 0.01$. Regime II kinetics is obeyed if $X = 2kg$ in the above equation leads to $Z \geq 1$. As pointed out by Lauritzen and Hoffman [30], the regime is judged based on whether the range of L -values calculated in each case is reasonable. If we assume $Z \leq 0.01$ and substitute $X = Kg$ into the Z test, the L -values are in the range of $9.6 \times 10^{-2} \text{ nm}$ for PBSA, which are unrealistic. Testing the $X = 2kg$ data for conformity to regime II led to L -values to be 27.89 nm for PBSA, which are reasonable for the structure of PBSA. Thus, it can be inferred that the crystallizations of PBSA and PBSA/m-LDH nanocomposites proceeded according to regime II.

The ΔH_f^0 and b -values of nanocomposites can be presumed to be the same as those of PBSA because the m-LDH content is low. The surface free energy ($\sigma\sigma_e$) data are estimated by means of Eq. (5) for PBSA and PBSA/m-LDH nanocomposites. As shown in Table 2, the $\sigma\sigma_e$ -value is 327.03 erg²/cm⁴ for PBSA, and those of the PBSA/m-LDH nanocomposites are calculated to be about 316.47, 315.08, and 321.11 erg²/cm⁴ for 1, 3, and 5 wt% loadings of m-LDH, respectively. The $\sigma\sigma_e$ -values of the PBSA/m-LDH nanocomposites are lower than those of PBSA. The value of $\sigma\sigma_e$ for the 3 wt% PBSA/m-LDH nanocomposites is the lowest in all the samples. This result indicates that the introduction of 3 wt% m-LDH content into PBSA causes an increase on the mobility of the PBSA chains [31]. However, in the case of the 5 wt% m-LDH, the $\sigma\sigma_e$ slightly increases as the content of m-LDH increases. Because the oleic acid and sorbitol serve as organo modifiers for LDH intercalation, m-LDH can obstruct the migration of PBSA chains.

Microstructures of PBSA and PBSA/m-LDH nanocomposites

To understand the microstructures of PBSA and PBSA/m-LDH nanocomposites, the SAXS technique is applied to investigate the change of morphology due to the addition of m-LDH. The Lorentz-corrected SAXS profiles of PBSA and PBSA/m-LDH nanocomposites isothermally crystallized at 52 °C are presented in Fig. 7a. Thus, the morphological parameters, such as long period (L_p), the average lamellar thickness (l_c), and the amorphous phase thickness ($l_a = L_p - l_c$) are determined by the following one-dimensional correlation function [32, 33]:

$$\gamma(z) = \frac{1}{Q} \int_0^\infty qI^2(q)\cos(qz)dq, \quad (8)$$

where z is the correlation distance, Q is a scattering invariant, and $I(q)$ is the experimental SAXS intensity corrected for thermal fluctuations.

The curves of one-dimensional correlation functions of PBSA and PBSA/m-LDH nanocomposites isothermally crystallized at 52 °C are shown in Fig. 7b. The data of L_p , l_c , and l_a are obtained from Fig. 7b. Table 3 summarizes the variations of L_p , l_c , and l_a for PBSA and PBSA/m-LDH nanocomposites. Clearly, the values of L_p and l_c for 1–3 wt% PBSA/m-LDH nanocomposites are slightly higher than that of PBSA. These results indicated that the incorporation of m-LDH can enhance the regular chain arrangement of PBSA. By increasing the content of m-LDH into PBSA up to 5 wt%, the L_p and l_c values slightly decrease as the content of m-LDH increases. These results reveal that the oleic acid and sorbitol chains of m-LDH inhibit the PBSA crystalline chain packing, which

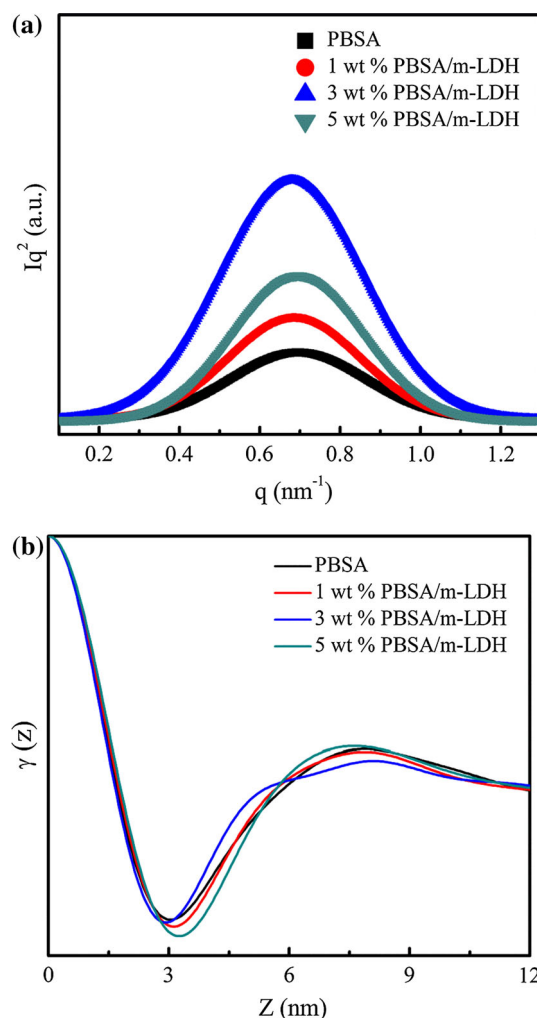


Fig. 7 **a** Lorentz-corrected SAXS intensity profiles and **b** one-dimensional correlation function calculated from the SAXS profiles for PBSA/m-LDH nanocomposites during isothermal crystallization at 52 °C

caused the decrease in the thickness of crystal layer and the increase in that of the amorphous layer.

Conclusions

A biodegradable PBSA/m-LDH nanocomposite has been prepared successfully via a solution-mixing process. The structures and morphologies of the PBSA/m-LDH nanocomposites characterized using WAXD and TEM demonstrate that most of the layered materials are exfoliated and randomly dispersed in the PBSA matrix. The isothermal crystallization kinetics of neat PBA and PBSA/m-LDH nanocomposite were analyzed using the Avrami equation. With the addition of 3 wt% m-LDH into PBSA, the half-time for crystallization of PBSA/m-LDH nanocomposite decreased by 47–76 % in the case of

Table 3 Structural parameters of PBSA and PBSA/m-LDH nanocomposites crystallized at T_c of 52 °C estimated from XRD and SAXS measurements

Sample	Temp. (°C)	X_c (%)	L_p (nm)	l_c (nm)	l_a (nm)
PBSA	52	52.19	7.86	5.29	2.57
1 wt% PBSA/m-LDH	52	52.62	7.89	5.43	2.46
3 wt% PBSA/m-LDH	52	53.66	8.11	5.68	2.43
5 wt% PBSA/m-LDH	52	53.28	7.61	5.02	2.59

isothermal crystallization at 48–56 °C compared to that of neat PBSA. In the presence of m-LDH, the spherulite size of PBSA nuclei decreased, and the number of spherulites increased substantially. Therefore, the addition of m-LDH to PBSA induces heterogeneous nucleation. The value of σ_e in the case of 3 wt% PBSA/m-LDH nanocomposites is the lowest. The microstructure of PBSA/m-LDH nanocomposites identified by SAXS shows that higher crystal layer thickness is achieved with the addition of 3 wt% m-LDH. These results indicate that the introduction of 3 wt% m-LDH content into PBSA causes a decrease in surface free energy and thus an increase in the polymer chain mobility.

Acknowledgement The financial support provided by Ministry of Science and Technology through the Project MOST 104-2212-E-005-089-MY2 is greatly appreciated.

References

- Bandyopadhyay J, Sinha Ray S (2010) The quantitative analysis of nano-clay dispersion in polymer nanocomposites by small angle X-ray scattering combined with electron microscopy. *Polymer* 51:1437–1449
- Nikolic MS, Djonlagic J (2001) Synthesis and characterization of biodegradable poly(butylene succinate-co-butylene adipate)s. *Polym Degrad Stab* 74:263–270
- Tserki V, Matzinos P, Pavlidou E, Vachliotis D, Panayiotou C (2006) Biodegradable aliphatic polyesters. Part I. Properties and biodegradation of poly(butylene succinate-co-butylene adipate). *Polym Degrad Stab* 91:367–376
- Ahn BD, Kim SH, Kim YH, Yang JS (2001) Synthesis and characterization of the biodegradable copolymers from succinic acid and adipic acid with 1,4-butanediol. *J Appl Polym Sci* 82:2808–2826
- Han SI, Lim JS, Kim DK, Kim MN, Im SS (2008) In situ polymerized poly(butylene succinate)/silica nanocomposites: physical properties and biodegradation. *Polym Degrad Stab* 93:889–895
- Hennous M, Derriche Z, Privas E, Navard P, Verney V, Leroux F (2013) Lignosulfonate interleaved layered double hydroxide: a novel green organoclay for bio-related polymer. *Appl Clay Sci* 71:42–48
- Bandyopadhyay J, Al-Thabaiti SA, Ray SS, Basahel SN, Mokhtar M (2014) Unique cold-crystallization behavior and kinetics of biodegradable poly[(butylene succinate)-co adipate] nanocomposites: a high speed differential scanning calorimetry study. *Macromol Mater Eng* 299:939–952
- Chen G, Yoon J-S (2005) Nanocomposites of poly[(butylene succinate)-co-(butylene adipate)] (PBSA) and twice-functionalized organoclay. *Polym Int* 54:939–945
- Ojijo V, Malwela T, Sinha Ray S, Sadiku R (2012) Unique isothermal crystallization phenomenon in the ternary blends of biopolymers polylactide and poly[(butylene succinate)-co-adipate] and nano-clay. *Polymer* 53:505–518
- Ikehara T, Kimura H, Qiu Z (2005) Penetrating spherulitic growth in poly(butylene adipate-co-butylene succinate)/poly(ethylene oxide) blends. *Macromolecules* 38:5104–5108
- Ojijo V, Sinha Ray S, Sadiku R (2012) Effect of nanoclay loading on the thermal and mechanical properties of biodegradable polylactide/poly[(butylene succinate)-co-adipate] blend composites. *ACS Appl Mater Interfaces* 4:2395–2405
- Ojijo V, Cele H, Sinha Ray S (2011) Morphology and properties of polymer composites based on biodegradable polylactide/poly[(butylene succinate)-co-adipate] blend and nanoclay. *Macromol Mater Eng* 296:865–877
- Wu CS (2012) Characterization and biodegradability of polyester bioplastic-based green renewable composites from agricultural residues. *Polym Degrad Stab* 97:64–71
- Kale G, Kijchavengkul T, Auras R, Rubino M, Selke SE, Singh SP (2007) Compostability of bioplastic packaging materials: an overview. *Macromol Biosci* 7:255–277
- Shah AA, Hasan F, Hameed A, Ahmed S (2008) Biological degradation of plastics: a comprehensive review. *Biotechnol Adv* 26:246–265
- Chen YA, Chen EC, Wu TM (2015) Organically modified layered zinc phenylphosphonate reinforced stereocomplex-type poly(lactic acid) nanocomposites with highly enhanced mechanical properties and degradability. *J Mater Sci* 50:7770–7778. doi:10.1007/s10853-015-9348-7
- Chen YA, Hang YT, Wu TM (2015) Polymorphism and spherulite morphology of poly(1,4-butylene adipate)/organically-modified layered double hydroxide nanocomposites. *J Appl Polym Sci*. doi:10.1002/app.42526
- Peng H, Han Y, Liu T, Tjiu WC, He C (2010) Morphology and thermal degradation behavior of highly exfoliated CoAl-layered double hydroxide/polycaprolactone nanocomposites prepared by simple solution intercalation. *Thermochim Acta* 502:1–7
- Ciou CY, Li SY, Wu TM (2014) Morphology and degradation behavior of poly(3-hydroxybutyrate-co-3-hydroxyvalerate)/layered double hydroxides composites. *Eur Polym J* 59:136–143
- Chiang MF, Chen EC, Wu TM (2012) Preparation, mechanical properties and thermal stability of poly(l-lactide)/ γ -polyglutamate-modified layered double hydroxide nanocomposites. *Polym Degrad Stab* 97:995–1001
- Lonkar SP, Singh RP (2009) Isothermal crystallization and melting behavior of polypropylene/layered double hydroxide nanocomposites. *Thermochim Acta* 491:63–70
- Hm Chen, Chen J, Ln Shao et al (2013) Comparative study of poly(L-lactide) nanocomposites with organic montmorillonite and carbon nanotubes. *J Polym Sci Pol Phys* 51:183–196
- Avrami M (1941) Granulation, phase change, and microstructure kinetics of phase change. III. *J Chem Phys* 9:177–184
- Avrami M (1940) Kinetics of phase change. II transformation-time relations for random distribution of nuclei. *J Chem Phys* 8:212–224

25. Alamo RG, Mandelkern L (1991) Crystallization kinetics of random ethylene copolymers. *Macromolecules* 24:6480–6493
26. Chen YA, Wu TM (2014) Crystallization kinetics of poly(1,4-butylene adipate) with stereocomplexed poly(lactic acid) serving as a nucleation agent. *Ind Eng Chem Res* 53:16689–16695
27. Hoffman JD, Weeks JJ (1962) Melting process and the equilibrium melting temperature of polychlorotrifluoroethylene. *J Res Natl Bur Stand A* 66:13–28
28. Hoffman JD (1983) Regime III crystallization in melt-crystallized polymers: the variable cluster model of chain folding. *Polymer* 24:3–26
29. Lauritzen JI, Hoffman JD (1973) Extension of theory of growth of chain-folded polymer crystals to large undercoolings. *J Appl Phys* 44:4340–4352
30. Lauritzen JI (1973) Effect of a finite substrate length upon polymer crystal lamellar growth rate. *J Appl Phys* 44:4353–4359
31. Causin V, Marega C, Saini R, Marigo A, Ferrara A (2007) Crystallization behavior of isotactic polypropylene based nanocomposites. *J Therm Anal Cal* 90:849–857
32. Strobl G, Schneider M (1980) Direct evaluation of the electron density correlation function of partially crystalline polymers. *J Polym Sci Polym Phys Ed* 18:1343–1359
33. Barbi V, Funari SS, Gehrke R, Scharnagl N, Stribeck N (2003) SAXS and the gas transport in polyether-block-polyamide copolymer membranes. *Macromolecules* 36:749–758